Fast subplasma membrane Ca2+ transients control exo-endocytosis of synaptic-like microvesicles in astrocytes

Published in final edited form as:
J Neurosci. 2008 September 10; 28(37): 9122–9132. doi:10.1523/JNEUROSCI.0040-08.2008.

Fast Subplasma Membrane Ca^{2+} Transients Control Exo-Endocytosis of Synaptic-Like Microvesicles in Astrocytes

Julie Marchaland[1,★], **Corrado Calì**[1,★], **Susan M. Voglmaier**[3], **Haiyan Li**[2], **Romano Regazzi**[1], **Robert H. Edwards**[2], and **Paola Bezzi**[1]

[1]Department of Cell Biology and Morphology, Faculty of Biology and Medicine, University of Lausanne, 1005 Lausanne, Switzerland [2]Department of Neurology and Physiology, University of California, San Francisco, San Francisco, California 94143 [3]Department of Psychiatry, University of California, San Francisco, San Francisco, California 94143

Abstract

Astrocytes are the most abundant glial cell type in the brain. Although not apposite for long-range rapid electrical communication, astrocytes share with neurons the capacity of chemical signaling via Ca^{2+}-dependent transmitter exocytosis. Despite this recent finding, little is known about the specific properties of regulated secretion and vesicle recycling in astrocytes. Important differences may exist with the neuronal exocytosis, starting from the fact that stimulus-secretion coupling in astrocytes is voltage independent, mediated by G-protein-coupled receptors and the release of Ca^{2+} from internal stores. Elucidating the spatiotemporal properties of astrocytic exo-endocytosis is, therefore, of primary importance for understanding the mode of communication of these cells and their role in brain signaling. We here take advantage of fluorescent tools recently developed for studying recycling of glutamatergic vesicles at synapses (Voglmaier et al., 2006; Balaji and Ryan, 2007); we combine epifluorescence and total internal reflection fluorescence imaging to investigate with unprecedented temporal and spatial resolution, the stimulus-secretion coupling underlying exo-endocytosis of glutamatergic synaptic-like microvesicles (SLMVs) in astrocytes. Our main findings indicate that (1) exo-endocytosis in astrocytes proceeds with a time course on the millisecond time scale ($\tau_{exocytosis} = 0.24 \pm 0.017$ s; $\tau_{endocytosis} = 0.26 \pm 0.03$ s) and (2) exocytosis is controlled by local Ca^{2+} microdomains. We identified submicrometer cytosolic compartments delimited by endoplasmic reticulum tubuli reaching beneath the plasma membrane and containing SLMVs at which fast (time-to-peak, ~50 ms) Ca^{2+} events occurred in precise spatial-temporal correlation with exocytic fusion events. Overall, the above characteristics of transmitter exocytosis from astrocytes support a role of this process in fast synaptic modulation.

Keywords

exocytosis; endocytosis; calcium; glutamate release; astrocytes; imaging

Introduction

Increasing evidence indicates that astrocytes are competent for regulated exocytosis and play a role in intercellular communication in the brain [for review, see Volterra and Meldolesi

Correspondence should be addressed to Dr. Paola Bezzi, Department of Cell Biology and Morphology, Faculty of Biology and Medicine, University of Lausanne, Rue du Bugnon 9, 1005 Lausanne, Switzerland. E-mail: Paola.Bezzi@unil.ch.
★J.M. and C.C. contributed equally to this work.

(2005) and Haydon and Carmignoto (2006)]. By responding to environmental stimuli with intracellular Ca^{2+} ($[Ca^{2+}]_i$) elevations and release of chemical transmitters (gliotransmitters) (Bezzi and Volterra, 2001), astrocytes are in the position to exchange a large variety of regulatory signals with surrounding cells. These findings constitute a conceptual breakthrough, although more work is needed to establish the exact contribution of astrocyte signaling to specific brain processes. A major obstacle to achieving this goal is the lack of a detailed description of the basic cell biological properties of astrocytes. The secretory aspect is a typical example. There is accumulating evidence that astrocytes secrete numerous transmitters by Ca^{2+}-dependent exocytosis (Bezzi et al., 2004; Zhang et al., 2004; Chen et al., 2005; Domercq et al., 2006; Bowser and Khakh 2007; Nadrigny et al., 2007). However, the available data are far from giving a complete and coherent description of the properties of the exo-endocytosis processes in astrocytes. Critical information is missing concerning the spatial-temporal characteristics of exocytosis, endocytosis recycling, and the underlying stimulus-secretion coupling mechanism. Moreover, further uncertainty is created by the emerging heterogeneity of the secretory pathways in astrocytes. Various types of organelles have been proposed to underlie exocytosis of gliotransmitters: from synaptic-like microvesicles (SLMVs) (Bezzi et al., 2004; Crippa et al., 2006; Jourdain et al., 2007), to dense-core granules (Coco et al., 2003; Striedinger et al., 2007), to lysosomes (Zhang et al., 2007), and to extra-large organelles with several μm long diameter (Xu et al., 2007). Past studies have not taken into account such heterogeneity. As a consequence, their descriptions of astrocytic secretion are probably not fully accurate, mixing contributions by more than one exocytic organelle population (Chen et al., 2005; Bowser and Khakh, 2007; Jaiswal et al., 2007; Nadrigny et al., 2007; Xu et al., 2007). Among the organelles putatively secreting gliotransmitters, glutamatergic SLMVs are the best and most extensively characterized. They have been identified both in adult brain tissue and in cell culture and studied at the ultrastructural as well as functional level (Bezzi et al., 2004; Crippa et al., 2006; Jourdain et al., 2007; Ni et al., 2007).

To define the specific characteristics of exo-endocytosis of glutamatergic SLMVs, we apply for the first time in astrocytes a strategy recently developed for studying the dynamics of glutamatergic synaptic vesicles (SVs) at synapses (Voglmaier et al., 2006). This consists of using the chimerical protein vesicular glutamate transporter 1 (VGLUT1)-pHluorin in combination with epifluorescence (EPI) and total internal reflection fluorescence (TIRF) illuminations (EPIi; TIRFi). VGLUT1-pHluorin combines the SLMV-specific targeting ensured by VGLUT1 to the properties of super-ecliptic pHluorin, a green fluorescent protein (GFP) with modified pH sensitivity (Miesenböck et al., 1998; Ryan and Reuter, 2001). When attached to the luminal domain of a vesicle resident protein, pHluorin allows a direct detection of fusion and retrieval of single vesicles (Sankaranarayanan and Ryan, 2000; Balaji and Ryan, 2007).

By using EPIi and TIRFi to monitor exo-endocytosis, respectively, at the whole-cell level and at the single-vesicle level, and dual-wavelength TIRF imaging for monitoring in parallel submembrane Ca^{2+} and SLMV dynamics, our study aims at (1) obtaining the first accurate kinetic description of exocytosis and endocytosis of astrocytic SLMVs and (2) defining the spatial-temporal characteristics of the underlying stimulus-secretion coupling mechanism.

Materials and Methods

Pharmacological agents, constructs, and transfection

All agents were from Sigma-Aldrich, unless otherwise indicated. Plasmids containing the VGLUT1-pHluorin and VGLUT1-mCherry constructs were prepared as described previously (Voglmaier et al., 2006); the endoplasmic reticulum (ER)-GFP plasmid was kindly provided by N. Demaurex (University of Geneva, Geneva, Switzerland) (Demaurex and Frieden, 2003). Each of these plasmids (0.5 μg for single transfection experiments or 0.25 μg for double

transfection experiments) was transfected into primary rat cortical astrocytes cultures with FuGene6 (3 μl; Roche Diagnostics).

Astrocyte cultures for imaging experiments

Astrocyte cultures containing >99% GFAP-positive cells (≤8% of which positive for the neural precursor marker LeX) were obtained from newborn rats. They were prepared as described previously (Bezzi et al., 2001), plated (2.5×10^4 cells) on glass coverslip and transfected 6–8 d later with VGLUT1-pHluorin, VGLUT1-mCherry or ER-GFP constructs. The double transfection protocol with VGLUT1-pHluorin and VGLUT1-mCherry resulted in an almost complete colocalization of the two fluorescent proteins (85 ± 11%). After transfection (2–5 d), coverslips were mounted in the open laminar flow perfusion incubator at 37°C (Harvard Apparatus) on the stage of a Zeiss Axiovert 200 fluorescence inverted microscope modified for TIRF and EPI experiments (Visitron System). The experimental chamber (250 μl volume) was perfused at a rate of 1–1.5 ml/min. The stimulus [(*RS*)-3,5-dihydrophenylglycine (DHPG); Tocris Bioscience] was applied rapidly (2 s) via a software-controlled microperfusion fast-step device (100 μl/min; Warner Instruments). Cells were perfused at 37°C in a HEPES-Krebs-Ringer HEPES (KRH) buffer containing (in m_M) 120 NaCl, 3.1 KCl, 2 $MgCl_2$, 1.8 $CaCl_2$, 1.25 NaH_2PO_4, 25 HEPES-Na (buffered to pH 7.4), glucose 4. Bafilomycin A1 (Baf A1) (Calbiochem) was used at a final concentration of 5 μ_M (diluted with HEPES-KRH) and incubated for 7–10 min before the stimulus. In experiments with thapsigargin (thapsi) or cyclopiazonic acid (CPA) (Calbiochem), the drugs were diluted in HEPES-KRH, incubated for 15–20 min, and the stimulus was subsequently applied when the Ca^{2+} signal recovered to basal level. SLMVs expressing VGLUT1-pHluorin were labeled by DHPG (2 s, 100 μ_M) in saline containing 15 μ_M FM 4–64 (Invitrogen).

For Ca^{2+} imaging experiments, cells (transfected or not transfected) were loaded with 5 μ_M of Fluo4 AM (Invitrogen) for 15 min or with 2.5 μg/ml of x-rhod-1 AM (Invitrogen) for 10 min in the presence of 0.02% pluronic F-127 (Invitrogen) at room temperature in the dark in a HEPES-KRH buffer, pH 7.4, and then de-esterified for 10–15 min before imaging.

Optical imaging

EPIi or TIRFi were alternatively used for our experiments. EPIi and TIRFi were alternated in real time for whole-cell pHluorin fluorescence (pHF) signal measurements in individual cells, in basal conditions and upon stimulation with DHPG. By imaging with excitation light at 488 nm generated by a 488 nm laser (20 mW; Laserphysics) and by a polychromator illumination system (Visichrome), the pHF signal was recorded at 10 Hz through a 100× objective lens (Zeiss; α-plan FLUAR 100X, 1.45 NA) and filtered with Zeiss filter set 10 (Zeiss).

TIRFi was used for all of the remaining experiments. The expanded beam of a 488/568 nm argon/krypton multiline laser (20 mW; Laserphysics) passed through an acousto-optic tunable filter laser wavelength selector (VisiTech International) synchronized with a soluble *N*-ethylmaleimide-sensitive factor attached protein-HQ charge-coupled device camera (Roper Scientific) under Metafluor software (Universal Imaging) control and was introduced to the coverslip from the high numerical aperture objective lens (α-plan FLUAR 100X; Zeiss). Light entered the coverslip and underwent total internal reflection at the glass-cell interface. In our experimental conditions, penetration depth of TIRFi was calculated by following, with some modifications, the method setup by Mattheyses and Axelrod (2006) to be ~92.12 nm. In single-wavelength TIRFi experiments (488 nm), the laser beam was filtered via the Zeiss filter set 10, and images were acquired at 20–40 Hz (Zeiss). In dual-wavelength TIRF illumination (488/568 nm), laser beams were combined by a dichroic mirror from the Zeiss filter 24 at 20–40 Hz. In TIRFi experiments, at which we monitored $[Ca^{2+}]_i$ events as fast as possible (40 Hz),

we restricted analysis to 10 regions of interest (ROIs) per cell located at different subdomains (i.e., in the processes and cell body). The pixel size was 126 nm (at binning 2).

Image analysis

Video images, digitized with MetaFluor, were analyzed with MetaMorph software (Universal Imaging). For details, refer to supplemental information, available at www.jneurosci.org as supplemental material.

Results

Kinetics of exo-endocytosis and reacidification of SLMVs in astrocytes

To study exo-endocytosis of astrocytic glutamatergic SLMVs, we transiently expressed VGLUT1-pHluorin in cultured astrocytes. Confocal analysis of the intracellular distribution of the VGLUT1-pHluorin showed that the protein mainly colocalized with endogenous cellubrevin (>90%) (supplemental Fig. 1 SI, available at www.jneurosci.org as supplemental material), endogenous glutamate (supplemental Fig. 3 SI, available at www.jneurosci.org as supplemental material), and partially overlapped with early or recycling endosomes (~20 and 30%, respectively), *trans*-Golgi network (~8%), and late endosomes/lysosomes (~6%) (Fig. 2 SI, available at www.jneurosci.org as supplemental material). By combining EPIi and TIRFi (10 Hz), we monitored pHF changes under basal conditions and upon stimulation of group I metabotropic glutamate receptors (mGluR) via local application of the specific agonist DHPG. The use of EPIi in real time with TIRFi was aimed at providing a comparative analysis of pHF changes in the whole cell and in its submembrane compartment. The sequence of images in Figure 1A shows that, under basal conditions, the pHF signal is very low both under TIRFi and EPIi; only a few fluorescent spots are visible, representing vesicles undergoing spontaneous discharge. Application of DHPG (100 μ_M, 2 s), which is known to trigger glutamate release from astrocytes (Bezzi et al., 1998, 2004), causes a rapid and transient increase in pHF consistent with exposure of the pHluorin epitope to the external pH (~7.4) in coincidence with vesicular fusions with the plasma membrane (Fig. 1 Aa–c). By placing a ROI on the whole-cell perimeter, we measured the kinetics of the DHPG-evoked pHF signal at the whole-cell level. Figure 1B compares the kinetics of the total pHF signal induced by DHPG under TIRFi and EPIi. In both cases, the rising phase of the signal is faster than its decay phase. However, under TIRFi, rise and decay time are significantly faster than under EPIi. To interpret this observation one has to take into account that the curve of the DHPG-evoked pHF signal represents at all times the net balance of exocytosis and endocytosis/reacidification (Sankaranarayanan and Ryan, 2000; Atluri and Ryan, 2006; Voglmaier et al., 2006). The rising phase indicates prevalent exocytosis and the decaying phase prevalent endocytosis and reacidification (Sankaranarayanan and Ryan, 2000; Schweizer and Ryan, 2006). On this basis, one can hypothesize that (1) the rise time of the DHPG-evoked pHF signal under TIRFi is faster than under EPIi because EPIi monitors vesicle reacidification processes occurring in cytosolic layers not accessible to TIRFi [penetration of the evanescent field (EW) in our apparatus is ~90 nm], and (2) the decay time under TIRFi is faster than under EPIi because endocytosed vesicles move out of the EW field before undergoing reacidification. To test these hypotheses, we performed “alkaline trapping” experiments to fully separate the three processes and determine their respective kinetics by using the V-type ATPase inhibitor Baf A1 (Sankaranarayanan and Ryan, 2000). Taken up by SVs during exocytosis, Baf A1 blocks the proton pump and prevents reacidification, trapping VGLUT1-pHluorin-expressing vesicles in the fluorescent state. Addition of Baf A1 thereby eliminates all changes of the pHF signal attributable to the reacidification component of recycling to reveal pure exocytosis. Astrocytes were exposed to 5 μ_M Baf A1, a dose known to completely inhibit extinction of the pHF signal in synaptic terminals (Sankaranarayanan and Ryan, 2001). As shown in Figure 1C, in the presence of Baf A1, under EPIi, DHPG evoked a nondecaying pHF signal that reached plateau

in 1.6 ± 0.33 s. Given that its rising phase corresponds to pure exocytosis, the slope of the linear fit represents the rate of the exocytic process (0.77 ± 0.056 A.U./s). By calculating the first derivative of the curve, we found that exocytosis reaches maximal speed at 800 ms (Fig. 1C, inset). This time represents the inflection point of the curve that indeed tends to have a flattened "S" shape, suggesting that exocytosis proceeds with an exponential time course for 800 ms and then gradually slows ($\tau_{riseEPIBaf\ 0–800\ ms}$ = 0.24 ± 0.017 s). Interestingly, in the presence of Baf A1, the TIRFi curve shows a rise time almost identical to the one of EPIi and comparable with those of TIRFi curves obtained in the absence of Baf A1 ($\tau_{riseTIRFBaf}$ = 0.25 ± 0.092 s vs $\tau_{riseTIRF}$ = 0.3 ± 0.088 s). These results confirm our hypothesis and indicates that (1) the difference between EPIi and TIRFi observed in the absence of the drug is attributable to reacidification occurring in the EPIi field but not in the TIRFi field and that (2) Baf A1 has no effect on both the rise and decay phases of the TIRFi ($\tau_{decayTIRF\ Baf}$ = 1.59 ± 0.09 s vs $\tau_{decayTIRF}$ = 1.63 ± 0.1 s) curve because vesicles escape the EW field before reacidification. Moreover, the identical slope observed in TIRFi and EPIi curves in the first 800 ms indicates the absence of vesicle movement out of the EW field (endocytosis) in this initial period. All of the parameters we calculated are summarized in supplemental Table 1, available at www.jneurosci.org as supplemental material.

We subsequently estimated reacidification (Fig. 1D; supplemental Fig. 2 SI, available at www.jneurosci.org as supplemental material) by subtracting the normalized EPIi curve in the absence of Baf A1 (Fig. 1B) from the one in the presence of the drug (Fig. 1C). During the stimulus, similarly to exocytosis, the reacidification proceeds with an exponential time course for 800 ms and then gradually slows (the curve shows a sigmoidal shape centered at 800 ms). The exponential fits allowed us to estimate the time constant of reacidification processes ($\tau_{rise\ 0–800\ ms}$ = 0.22 ± 0.02 s) that, based on the previous results, are detected only by EPIi and involved pool of vesicles located deep in the cytoplasm and out of the EW field. The poststimulus reacidification instead displays a linear increase reaching a plateau in ~10 s (0.052 ± 0.0008 A.U./s). We finally estimated endocytosis (Fig. 1E; supplemental Fig. 2 SI, available at www.jneurosci.org as supplemental material) by subtracting the normalized TIRFi curve from the normalized EPIi curve, both obtained in the presence of Baf A1 (Fig. 1C). The endocytosis starts 600 ÷ 800 ms after the stimulus, proceeds with an exponential time course for 400 ÷ 600 ms, to then gradually decline ($\tau_{rise\ 800–1200\ ms}$ = 0.26 ± 0.03 s). Interestingly, by calculating the first derivative (Fig. 1E, inset), we found that the endocytosis curve contains two inflection points at 1.2 s and at 2.8 s ($\tau_{rise\ 2000–2800\ ms}$ = 1 ± 0.25 s), suggesting the presence of two distinct phases of endocytosis. The rates of endocytosis during and after the stimulus were estimated by linear fitting (0.8–2 s, 0.66 ± 0.025 A.U./s; >2 s, 0.16 ± 0.005 A.U./s) (see Fig. 6).

In the subsequent set of experiments, we confirmed that exo-endocytosis is controlled by the intensity of G-protein-coupled receptor (GPCR) stimulation as the peak value of the pHF signal varied with the dose of agonist (Fig. 1F). Moreover, we found that the process requires release of Ca^{2+} from internal stores. Indeed, the DHPG-evoked pHF signal was abolished by inhibition of the ER Ca^{2+}-ATPase by either thapsi [−91.7 ± 2.7%; 50 nM, 20 min; n = 10 cells, 5 experiments (exps)] or CPA (−80.6 ± 6.6%; 10 μM, 15 min; n = 8 cells, 4 exps).

Kinetic analysis at the single vesicle level

To study the kinetics of exo-endocytosis at the level of individual SLMVs, we performed experiments under TIRFi that, producing an EW, in our set-up excites fluorophores within 80–90 nm from the plasma membrane (Domercq et al., 2006). Astrocytes were transfected with two different constructs: VGLUT1 coupled to mCherry (red, VGLUT1-mCherry), labeling the SLMV membrane, and VGLUT1-pHluorin (green), signaling exocytic fusion of the SLMV (Tsuboi and Rutter, 2003).

By using a dual wavelength TIRF (568/488 nm), we then monitored (at 20 Hz) individual double-fluorescent SLMVs and evaluated their emission intensities in both a small circle around the vesicle and a concentric annulus around the circle (Bezzi et al., 2004). Under basal conditions, the vast majority (97.4%) of the observed fusion events fell into two well-defined and distinct categories (subtype 1 and subtype 2 events). Subtype 1 events accounted for 63% of the events (n = 26 cells). They were characterized by the abrupt appearance in the EW field of the pHF signal that remained constant for 400 ms to then disappear without any significant lateral diffusion (Fig. 2A). VGLUT1-mCherry fluorescence (mCF), already present in the EW field at the appearance of the pHF signal, remained constant (approximately −0.01% of $\Delta F/F_0$) during the 400 ms of the fusion event, and then disappeared together with the pHF signal. We interpret the simultaneous disappearance of the two fluorescent markers as a movement of the SLMV out of the EW field. Moreover, the fact that, during the fusion event, both markers were retained in the vesicle membrane strongly suggests a “kiss-and-run” mode of exo-endocytosis (Fesce et al., 1994) (Fig. 2A, diagram). SLMVs (8.7%) showing a subtype 1 fusion displayed a much longer increase of fluorescence (up to 7.5 s) before returning to basal level.

In the case of a subtype 2 event, fusion lasted longer and proceeded differently. The pHF signal, once it appeared, started to diffuse in the external annulus and was diluted out in ~700 ms; in parallel, the mCF signal progressively decreased in intensity (−86 ± 0.7% of $\Delta F/F_0$ in 400 ms; n = 475; $p < 0.05$, unpaired t test) (Fig. 2B). These two combined events suggest that the SLMV loses its identity by mixing with the plasma membrane and undergoes a classical “full-collapse” type of fusion (Fig. 2B, diagram).

To confirm that increases in pHF signal depended on exocytic fusion of SLMVs with the plasma membrane, we performed a parallel set of experiments using VGLUT1-pHluorin-transfected astrocytes bathed in external medium containing FM 4–64, an amphipathic dye that loads into vesicles only when they fuse with the plasma membrane (Gaffield and Betz, 2006). Indeed, in all of the cases when a pHF signal appeared, the FM dye immediately started to accumulate in the SLMV membrane (Fig. 2A,B, bottom). Its fluorescence remained visible throughout the duration of the pHF signal and eventually disappeared with it, indicating that FM 4–64 was taken up by the fused vesicle and followed its fate.

Subsequently, we studied the time distribution of the individual fusion events evoked by GPCR stimulation in the doubly transfected cells. Figure 2C shows that application of DHPG triggered a burst of exocytosis comprising two phases: a rapid one, peaking at 200–300 ms, and a slower one, peaking at 400–600 ms. We used the mCF signal to subdivide SLMVs into “residents” (vesicles present in the EW field before the stimulus) and “newcomers” (vesicles whose mCF signal appeared in the EW after the stimulus) (Zenisek et al., 2000). We found that SLMVs undergoing exocytosis during the rapid phase (0–400 ms) were mostly residents (83%, corresponding to 42% of the total number of DHPG-evoked fusion events; n = 8400), whereas vesicles undergoing exocytosis during the slow phase (500 ms–1.6 s) were almost all newcomers (88%), possibly representing recycling vesicles (Fig. 2D). Interestingly, the majority of resident SLMVs that fused underwent subtype 1 (92.5%), whereas the majority of newcomer SLMVs that fused underwent subtype 2 (84.6%).

Spatial relationship between ER and SLMVs

The spatial-temporal characteristics of the $[Ca^{2+}]_i$ signals triggering exocytosis in astrocytes have not yet been investigated. According to previous study, somatic $[Ca^{2+}]_i$ elevations in response to GPCR activation peak within 1–2.5 s from stimulation (Fiacco and McCarthy, 2006). Therefore, these signals are too slow to underlie the exo-endocytosis processes reported here. Considering that SLMV exocytosis takes place on a millisecond time-scale and depends on Ca^{2+} release from internal stores, one would predict the existence of localized ER-dependent $[Ca^{2+}]_i$ events near the fusion sites. As a consequence, we predicted that ER tubuli lie close to

SLMVs and in proximity of the cell plasma membrane. To directly verify this possibility, we labeled the ER tubuli by transfecting astrocytes with ER-GFP, a construct that targets GFP expression to the ER (Demaurex and Frieden, 2003). Figure 3A shows that the ER in astrocytes is a continuous network of tubuli and cisternae. Under TIRFi, the fluorescent structures appear discrete, consisting of tubular tips approaching the plasma membrane (Fig. 3B). Cotransfection of ER-GFP and VGLUT1-mCherry revealed an extensive overlay of ER and SLMVs, demonstrated by the close proximity of most of the red dots (~87%) to the green ER structures (Fig. 3B). By means of a cross-correlation analysis performed at the all-cell level, we found that ER and SLMVs are spatially correlated (supplemental Fig. 8 SI, available at www.jneurosci.org as supplemental material). For a detailed analysis, we then focused on red dots corresponding to individual SLMVs (supplemental Fig. 6 SI, available at www.jneurosci.org as supplemental material). A line of fluorescence intensity profile was traced across any given red dot and its closest green structure to analyze their fluorescence distribution and to extrapolate the interdistance between ER and SLMV (supplemental Fig. 7 SI, available at www.jneurosci.org as supplemental material, and image analysis SI, available at www.jneurosci.org). The most frequent result (47 ± 7.5% of cases; $n = 6$ cells) was an SLMV and ER tubuli located side by side (Fig. 3B, case 1). Their fluorescence curves typically overlapped, indicating that ER and SLMV were located within a distance smaller than the point spread function of our microscope. Their average interdistance interval was 375 ± 185 nm. Another frequent situation (31.4 ± 5.9% of cases) was the alignment of SLMV and ER on the *z*-axis, as shown by the complete overlap of the two intensity profiles despite a difference in intensity between corresponding peaks (Fig. 3B, case 2). In a small number of cases (8.4 ± 7.4%), the ER-GFP profile had a "donut-shaped" distribution with a central dimple occupied by the VGLUT1-mCherry-expressing vesicle (Fig. 3B, case 3). Taking into account that our study was performed in the limited submembrane field illuminated by TIRF, we conclude that ER tubuli and SLMVs, together with the plasma membrane, delimit submicrometer cytosolic compartments.

Subplasma membrane Ca^{2+} events

Given the presence of ER tubuli together with SLMVs just beneath the plasma membrane, we subsequently used TIRFi imaging (488 nm, 20 Hz) to selectively investigate submembrane Ca^{2+} signals occurring in the EW field (Steyer and Almers, 2001). Experiments were performed on nontransfected astrocytes loaded with a green $[Ca^{2+}]_i$ indicator, Fluo4-AM, and Ca^{2+} signals studied both under basal conditions and upon GPCR stimulation with DHPG. For analysis, we divided the cell profile appearing under TIRFi in small equal-sized (4 μm^2) squared regions, each of which could contain one SLMV and its surrounding ER structure (supplemental Fig. 9A SI, available at www.jneurosci.org as supplemental material). At first, we compared the average submembrane fluorescence signal (F) in 1 s periods taken before, during, and after stimulation with DHPG. F corresponds to the mean fluorescence value given by the sum of the signals from individual regions divided by the number of regions. In the presence of DHPG, F was significantly higher than in the periods immediately preceding and after the stimulation, indicating that mGluR stimulation triggers elevation of submembrane Ca^{2+} (supplemental Fig. 9B SI, available at www.jneurosci.org as supplemental material) (DHPG, 234.32 ± 2.92 F; before, 203.02 ± 0.86 F; after, 218.33 ± 0.82 F; $n = 1275$ traces in 15 cells; $p < 0.05$, multiple-comparison ANOVA). We then proceeded to define the spatial-temporal characteristics of individual submembrane Ca^{2+} events. By means of a retrospective analysis, we centered the ROIs on each visualized Ca^{2+} signal and analyzed the fluorescence traces. The submembrane Ca^{2+} signals have been expressed has ΔF ($F - F_0$) divided by F_0, in which the F_0 is the mean of ~1 s of the basal level in each respective ROI before the stimulus (supplemental Fig. 10 SI, available at www.jneurosci.org as supplemental material; Image analysis SI, available at www.jneurosci.org). As shown in Figure 4A, very rapid, spike-like Ca^{2+} events were easily distinguishable. By acquiring images at 40 Hz, we highlighted the morphology of such spiking

Ca^{2+} events and established that most of them last ~150 ms and peak at 50 ms (n = 583 traces from five cells) (Fig. 4A, insert). Under basal conditions, the frequency of the rapid submembrane Ca^{2+} events was very low (0.87 ± 0.34/s/ROI; n = 1005 events in 25 cells). Application of DHPG induced within 300 ms an ~4-fold increase of their mean frequency (3.45 ± 1.13/s/ROI; n = 6706 events in 25 cells; $p < 0.05$, unpaired t test). It also increased their mean amplitude by ~1.7-fold (1.62 ± 0.72 basal vs 2.8 ± 0.7 stimulated $\Delta F/F_0$; n = 6706 events in 25 cells; $p < 0.05$, unpaired t test) but did not modify their temporal profile. In parallel, we evaluated the propagation of the spiking Ca^{2+} signals in the x–y plane by following the lateral spread of fluorescence in three concentric ROIs (diameter: 2, 4, and 6 μm, respectively) centered on each Ca^{2+} signal. The diameter of most of the Ca^{2+} events was $\leq$3 μm. The average diameter (1.75 ± 0.18 μm) was increased by DHPG application (2.5 ± 0.34 μm; $p < 0.05$, unpaired t test). Interestingly, we noticed that DHPG induced a small fraction (~7.5%) of the Ca^{2+} events to propagate at long distance (up to 14 μm) from the ROI in which they originate, causing a submembrane Ca^{2+} wave (data not shown). Our results indicate that submembrane Ca^{2+} events are generally short lived and spatially confined. Their specific characteristics in terms of amplitude ($\Delta F/F_0$ maximum), kinetics, and lateral propagation are summarized in Figure 4B. The temporal distribution of the submembrane Ca^{2+} events evoked by DHPG application is shown in Figure 4C. Such a distribution corresponds to a biphasic burst in all similar to the one observed for the exocytic events (Figs. 2C; 4C, ghost). Indeed, DHPG-evoked Ca^{2+} and exocytic events were found to be strictly temporally correlated; in particular, each one of the two peaks of Ca^{2+} events preceded the corresponding peak of exocytic events by an interval of ~100 ms.

Finally, with pharmacological experiments shown in Figure 4D, we confirmed that submembrane Ca^{2+} events depend exclusively on Ca^{2+} released from internal stores. Thus, the number of events remained unchanged when we removed Ca^{2+} from the incubation medium (0 Ca^{2+} with 5 mM EGTA) or added nifedipine (3 μM), a blocker of L-type voltage-gated Ca^{2+} channels. In contrast, the number of events increased during the first 15 s of incubation with CPA (approximately by 3.8-fold) (supplemental Fig. 11 SI, available at www.jneurosci.org as supplemental material) and returned to a baseline value between 1 and 7 min (0.76 ± 0.25/s/ROI) and eventually almost completely disappeared in ~10 min (0.095 ± 0.014/s/ROI). After 15 min of incubation with CPA, application of DHPG failed to induce submembrane Ca^{2+} events (Fig. 4D). These results constitute the first evidence of spatially confined, ER-mediated submembrane Ca^{2+} events occurring in astrocytes on a millisecond time scale.

Spatial and temporal correlation between submembrane Ca^{2+} events and SLMV exocytic events

To directly prove that fast submembrane Ca^{2+} elevations are the events triggering exocytosis of SLMVs, we monitored the two types of event simultaneously and defined their spatial and temporal correlation. First, we focused on the spatial aspect. Astrocytes were transfected with VGLUT1-mCherry, loaded with Fluo4-AM, and imaged under dual wavelength TIRFi (488/568 nm, 40 Hz). To monitor Ca^{2+} events at the maximal possible speed, we restricted sampling to 10 ROIs randomly selected at different cell locations, in both the cell body and the processes. ROIs (6 μm^2) were centered on an individual SLMV, identified by its mCF signal (supplemental Fig. 1 SI, available at www.jneurosci.org as supplemental material). When we stimulated with DHPG, spike-like submembrane Ca^{2+} events (1.6 ± 0.5/s/ROI; n = 250 ROI in 25 cells) identical to those observed previously in nontransfected cells appeared in the ROIs (average time to peak, 58.6 ± 8.2 ms; diameter, 2.1 ± 1.6 μm; n = 1340 traces from 10 cells) (Fig. 5A). Interestingly, by means of cross-correlation analysis, we found that the submembrane Ca^{2+} events, similarly to the ER structures, occurs in strict spatial correlation with submembrane sites SLMVs (those most probably representing the ready to fuse vesicles)

(supplemental Fig. 8 SI, available at www.jneurosci.org as supplemental material). For detailed analysis, we then traced a line of fluorescence intensity profile over the mCF signal and the closest Fluo4 fluorescence signal. Practically, in all cases that we analyzed (96.4 ± 2.4%; n = 250 pairs in 25 cells) (Fig. 5A), the two curves overlapped for >75% and their peaks had an average interdistance of 245 ± 8.3 nm. Interestingly, in some cases (12.6% of pairs), the $[Ca^{2+}]_i$ event showed a "donut-shape distribution" (reminiscent of the ER distribution around SLMV) in which the fluorescence intensity profiles of the mCF were bell shaped, whereas those of Fluo-4 showed humps on both sides of the SLMV profile, suggesting that $[Ca^{2+}]_i$ rises to highest levels around the vesicular organelle.

Subsequently, we considered the temporal aspect. Individual Ca^{2+} events and single SLMV fusions were monitored in parallel, the latter revealed by VGLUT1-pHluorin, the former by the red calcium indicator x-rhod-1-AM (488/568 nm, 20 Hz). To compensate for the fact that x-rhod gives a smaller ΔF than Fluo4 for the same $\Delta[Ca^{2+}]$, we restricted our analysis to ROIs selected in the cell regions with highest signal-to-noise ratio (i.e., the cell processes and the border of the cell body). In 28 cells stimulated with DHPG, we most often observed (65% of 225 cases) a Ca^{2+} event rapidly followed (≤3 frames) by a fusion event (Fig. 5B). In only 20% of cases, the Ca^{2+} event was not followed by a detectable fusion event in the same ROI, and in 15% of cases, the fusion event was not preceded by a Ca^{2+} event. The averaged kinetics of Ca^{2+} and fusion events in Figure 5C show a strict temporal correlation, with the Ca^{2+} peak preceding the pHF peak by 57.9 ± 4.5 ms (n = 35 from 10 cells). Importantly, when we depleted the ER Ca^{2+} stores with CPA, we observed a dramatic reduction of both submembrane Ca^{2+} events and SLMV fusion events (−85 ± 14% and −89 ± 12%, respectively; n = 102 ROIs in 12 cells), implying that the two types of event are causally related. Overall, our observations indicate that exocytosis of SLMVs in response to GPCR stimulation is sustained by fast, local Ca^{2+} elevations mediated by Ca^{2+} release from the ER and suggest for the first time that the stimulus-secretion coupling in astrocytes occurs at the level of functional microdomains.

Discussion

Characteristics of SLMV exocytosis and endocytosis in astrocytes

Although it is increasingly clear that astrocytes express multiple populations of secretory organelles, imaging studies performed to date used generic fluorescent markers of exocytosis that do not distinguish among populations. The simultaneous recording of fusion signals from distinct populations of secretory organelles may lead to significant discrepancies in the kinetic values of exocytosis (Bezzi et al., 2004; Chen et al., 2005; Bowser and Khakh, 2007; Jaiswal et al., 2007). In the present study, we took advantage of VGLUT1-pHluorin to overcome limitations of previous works. Indeed, the intracellular distribution of VGLUT1-pHluorin showed that the vast majority of the GFP-labeled vesicles were positive for a SNARE (soluble *N*-ethylmaleimide-sensitive factor attachment receptor) protein cellubrevin (Bezzi et al., 2004; Crippa et al., 2006), displayed a diameter compatible with SLMVs in other secretory cells and release glutamate (supplemental Figs. 1 SI, 2 SI, 3 SI, 5 SI, available at www.jneurosci.org as supplemental material). We performed several sets of experiments to investigate spatial and temporal relations between $[Ca^{2+}]_i$ and exocytosis processes in astrocytes.

At first, we defined the kinetics of exocytosis, endocytosis, and reacidification at the whole-cell level (Fig. 1). A major challenge consisted in separating the exocytosis and the two components of the endocytic process: the movement of the recently fused vesicles from plasma membrane to cytoplasm (out of the EW field) and the reacidification process. This was achieved with alkaline trapping experiments in that we isolated the exocytosis signal by blocking reacidification with the proton pump inhibitor Baf A1 (Sankaranarayanan and Ryan, 2001). In the presence of Baf A1, the rising phase under EPIi represented a pure measure of exocytosis

(Fig. 1C). Comparison with the EPIi signal in the absence of Baf A1 enabled us to calculate the cumulative amount of reacidification by calculating the difference between the two (Fig. 1D); the resulting "difference curve" provided the complete kinetic of reacidification during and after the stimulus. Interestingly, in the first 800 ms, we calculated a fast rate of reacidification ($\tau = 0.22 \pm 0.02$) (Fig. 1D) that occurs in pool of vesicles located out of the EW field. The fast reacidification proceeds with a time course similar to exocytosis and most likely represents a mechanism responsible for uptake glutamate into the cytosolic pool of SLMVs.

By comparing the normalized EPIi and TIRFi curves in the presence of Baf A1, we then calculated the kinetic of the movement of SLMVs out of EW field (the first step of the endocytosis) (Fig. 1E). The first derivative of the endocytosis curve shows the evolution of the speed of endocytic events (Fig. 1E, inset); they start at ~600 ms, reach two maxima at 1.2 s, and at 2.8 s to then end after ~6 s. The bimodal distribution indicates the existence of two distinct phases of endocytosis. By directly comparing the kinetics of endocytosis and exocytosis (Fig. 6), we found that during the stimulus, the rate of endocytosis was more than half that of exocytosis (Endo/Exo, 0.85), indicating that SLMV retrieval proceeds fast enough to compensate for exocytosis (Fernández-Alfonso and Ryan, 2004).

In the second set of experiments we performed the analysis at the single vesicle level with TIRFi (Fig. 2). The fast imaging protocol applied in these sets of experiments provided new informations on the kinetic and modalities of exocytosis and recycling.

We found that the exocytic burst, similar to endocytosis, displayed a bimodal distribution (Fig. 2C), strongly suggesting the existence of two modes of exo-endocytosis. We confirmed this hypothesis with a double transfection approach in that we could directly visualize the fate of SLMVs during exocytosis and retrieval (Fig. 2A,B,D). Indeed, we noticed heterogeneity both in the origin of the SLMVs that underwent exocytosis (Fig. 2D, residents vs newcomers) and in their mode of fusion (kiss-and-run vs full-collapse type of fusion). The rapid phase of the exocytic burst (0–400 ms) was sustained almost exclusively by resident vesicles undergoing kiss-and-run fusion, whereas the slow phase (500 ms–1.6 s) mainly by newcomer vesicles undergoing full-collapse fusion. This duality is reminiscent of observations in neurons in that only readily releasable SVs are rapidly recycled and reused (Harata et al., 2006). Our experiments do not clarify whether newcomers and resident vesicles represent distinct population of SLMVs. The newcomers may indeed represent the same population of resident vesicles that undergo a second round of exocytosis upon rapid recycling. In previous studies in which we used acridine orange (AO) as a fluorescent reporter of fusion events, DHPG stimulation induced a single monophasic burst of exocytosis, much shorter (~500 ms) than the one observed here (Bezzi et al., 2004;Domercq et al., 2006). In light of the present observations, it is possible that the release of AO in the external medium upon vesicle fusion prevented us from detecting exocytic events of recycled vesicles.

What can be the functional significance of the two modalities of secretion detected in astrocytes?

Studies in synaptic terminals indicate that full-collapse fusion (Heuser and Reese, 1973) and kiss-and-run (Fesce et al., 1994) coexist and play active roles in exocytic events. In particular, in small nerve terminals, kiss-and-run has an additional role of enabling nerve terminals to respond to high-frequency inputs with a scarce number of vesicles. In astrocytes, it is possible that, such as at nerve terminals, the two modalities of fusion can each contribute to maintain cellular communication over a wide range of different stimuli. Further studies are necessary to address this point.

Subplasma membrane Ca^{2+} microdomains regulate SLMV exocytosis in astrocytes

The present study addresses for the first time whether localized microdomains of Ca^{2+} control fusion events in astrocytes. Previous studies that monitored Ca^{2+} responses to GPCR activation focused on bulk $[Ca^{2+}]_i$ changes, in general limiting their observations to the somatic cell region (Pasti et al., 1997; Bezzi et al., 1998; Pasti et al., 2001; Fiacco and McCarthy, 2006). Such Ca^{2+} elevations normally peaked within 1–2 s from stimulation and thus are too slow to underlie the rapid burst of exocytosis described here.

Here, by using TIRFi, we observed that localized domains of Ca^{2+} exist at or near the sites of exocytosis. ER tubules and cisterns come in tight apposition of the plasma membrane, with a complex spatial arrangement that delimits tiny structural domains of submicrometer space (femtoliter). Such a spatial organization most likely limits diffusion of signaling molecules, including Ca^{2+}. Moreover, ER structures and SLMVs lie in the submembrane compartments in tight spatial proximity, with an average distance of 300–500 nm. These results are in line with recent observations in that ER tubules have been considered to be distinct compartments, structurally and functionally coupled to the plasma membrane via cytoskeletal scaffold proteins (Tse et al., 1997; Blaustein and Golovina, 2001; Sala et al., 2005; Wu et al., 2006). In this respect, the organization of cytoskeleton in astrocytes could be similar to those at glutamatergic synapses, in which the scaffold protein Homer provides a molecular link between IP_3 receptors at the tip of the ER cisternae and mGluRs on the plasma membrane (Tu et al., 1998; Xiao et al., 1998; Sala et al., 2005).

What is the functional implication of the subplasma membrane ER domains? We found that stimulation of group I mGluRs generates store-dependent submicrometer Ca^{2+} events characterized by fast kinetics (50–150 ms) and spatial segregation ($\leq 3\ \mu m$).

Importantly, in most cases Ca^{2+} events occurred at or near sites in which SLMVs underwent exocytosis ($\leq$280 nm) and were in strict temporal and spatial correlation with fusion events (supplemental Fig. 8 SI, available at www.jneurosci.org as supplemental material). Indeed, Ca^{2+} and exocytosis displayed similar, biphasic distribution, with the Ca^{2+} peaks preceding the corresponding exocytosis peaks of ~100 ms.

The typology of the subplasma membrane Ca^{2+} events observed in astrocytes is strongly reminiscent of the so-called "Ca^{2+} puffs" (Thomas et al., 2000; Bootman et al., 2001) that typically consist of a fast elevation of the $[Ca^{2+}]_i$ and limited spatial spread (Rizzuto and Pozzan, 2006). As for the astrocytic signals, we do not know whether their spatial characteristics reflect the clustering of IP_3Rs along the ER structures or the clustering of receptors along the plasma membrane, or both. The cumulative recruitment of Ca^{2+} puffs can lead to the initiation and propagation of a global cytosolic Ca^{2+} signal (Tovey et al., 2001). This may also occur in astrocytes; in limited cases, we observed long-distance (several μm) propagation of the Ca^{2+} events from the site of origin along the subplasma membrane, in the form of a submembrane Ca^{2+} wave. Moreover, in view of the limited depth of the TIRFi field, we cannot exclude that Ca^{2+} events propagate also in the *z*-axis.

How do subplasma membrane Ca^{2+} events control SLMV exo-endocytosis in astrocytes? In resting conditions, Ca^{2+} events display spontaneous oscillatory patterns that upon stimulation with DHPG increase in both the amplitude and the frequency (~2- and 4-fold). However, at present, we cannot say whether one of the two plays a predominant role in triggering exocytosis.

Are these findings relevant to understanding the functional role of transmitter release from astrocytes in brain function? A few studies performed *in vivo* to date demonstrate that astrocytes respond to neuronal activity with slow and long-lasting $[Ca^{2+}]_i$ elevations, peaking within seconds from neuronal stimulation (Hirase et al., 2004; Nimmerjahn et al., 2004; Wang et al.,

2006). A recent study, however, shows for the first time the occurrence *in vivo* of fast astrocytic Ca^{2+} events in response to neuronal activity, peaking in the millisecond time scale from sensory stimulation (Winship et al., 2007). This finding suggests that the fast Ca^{2+} events here identified are not a peculiarity of astrocytes in cell culture but may correspond to events taking place in astrocytes of the living brain. Establishing whether fast Ca^{2+} events *in vivo* are associated to transmitter release via SLMV exocytosis becomes, therefore, of the outmost importance to define the type of modulatory influence exerted by astrocytes on neighboring neuronal circuits.

Supplementary Material

Refer to Web version on PubMed Central for supplementary material.

Acknowledgments

This work was supported by a Faculty of Biology and Medicine 2006 grant, University of Lausanne, Lausanne, Switzerland (P.B.). We thank R. Tsien for providing the mCherry construct and N. Demaurex for providing the ER-GFP; O. Mirante and P. Spagnuolo for experimental support; M. Giugliano, S. Vesce, V. Schubert, and M. Santello for scientific discussions; and J. Meldolesi, O. Kochubey, N. Korogod, and A. Volterra for comments and revisions on this manuscript.

References

Atluri PP, Ryan TA. The kinetics of synaptic vesicle reacidification at hippocampal nerve terminals. J Neurosci 2006;26:2313–2320. [PubMed: 16495458]

Balaji J, Ryan TA. Single-vesicle imaging reveals that synaptic vesicle exocytosis and endocytosis are coupled by a single stochastic mode. Proc Natl Acad Sci U S A 2007;104:20576–20581. [PubMed: 18077369]

Bezzi P, Carmignoto G, Pasti L, Vesce S, Rossi D, Rizzini BL, Pozzan T, Volterra A. Prostaglandins stimulate calcium-dependent glutamate release in astrocytes. Nature 1998;391:281–285. [PubMed: 9440691]

Bezzi P, Domercq M, Brambilla L, Galli R, Schols D, De Clercq E, Vescovi A, Bagetta G, Kollias G, Meldolesi J, Volterra A. CXCR4-activated astrocyte glutamate release via TNFalpha: amplification by microglia triggers neurotoxicity. Nat Neurosci 2001;4:702–710. [PubMed: 11426226]

Bezzi P, Gundersen V, Galbete JL, Seifert G, Steinhauser C, Seifert G, Steinhäuser C, Pilati E, Volterra A. Astrocytes contain a vesicular compartment that is competent for regulated exocytosis of glutamate. Nat Neurosci 2004;7:613–620. [PubMed: 15156145]

Blaustein MP, Golovina VA. Structural complexity and functional diversity of endoplasmic reticulum Ca($^{2+}$) stores. Trends Neurosci 2001;24:602–608. [PubMed: 11576675]

Bootman MD, Lipp P, Berridge MJ. The organisation and functions of local Ca($^{2+}$) signals. J Cell Sci 2001;114:2213–2222. [PubMed: 11493661]

Bowser DN, Khakh BS. Two forms of single-vesicle astrocyte exocytosis imaged with total internal reflection fluorescence microscopy. Proc Natl Acad Sci U S A 2007;104:4212–4217. [PubMed: 17360502]

Chen X, Wang L, Zhou Y, Zheng LH, Zhou Z. "Kiss-and-run" glutamate secretion in cultured and freshly isolated rat hippocampal astrocytes. J Neurosci 2005;25:9236–9243. [PubMed: 16207883]

Coco S, Calegari F, Pravettoni E, Pozzi D, Taverna E, Rosa P, Matteoli M, Verderio C. Storage and release of ATP from astrocytes in culture. J Biol Chem 2003;278:1354–1362. [PubMed: 12414798]

Crippa D, Schenk U, Francolini M, Rosa P, Verderio C, Zonta M, Pozzan T, Matteoli M, Carmignoto G. Synaptobrevin2-expressing vesicles in rat astrocytes: insights into molecular characterization, dynamics and exocytosis. J Physiol 2006;570:567–582. [PubMed: 16322057]

Demaurex N, Frieden M. Measurements of the free luminal ER Ca($^{2+}$) concentration with targeted "cameleon" fluorescent proteins. Cell Calcium 2003;34:109–119. [PubMed: 12810053]

Domercq M, Brambilla L, Pilati E, Marchaland J, Volterra A, Bezzi P. P2Y1 receptor-evoked glutamate exocytosis from astrocytes: control by tumor necrosis factor-alpha and prostaglandins. J Biol Chem 2006;281:30684–30696. [PubMed: 16882655]

Fernández-Alfonso T, Ryan TA. The kinetics of synaptic vesicle pool depletion at CNS synaptic terminals. Neuron 2004;41:943–953. [PubMed: 15046726]

Fesce R, Grohovaz F, Valtorta F, Meldolesi J. Neurotransmitter release: fusion or 'kiss-and-run'? Trends Cell Biol 1994;4:1–4. [PubMed: 14731821]

Fiacco TA, McCarthy KD. Astrocyte calcium elevations: properties, propagation, and effects on brain signaling. Glia 2006;54:676–690. [PubMed: 17006896]

Gaffield MA, Betz WJ. Imaging synaptic vesicle exocytosis and endocytosis with FM dyes. Nat Protoc 2006;1:2916–2921. [PubMed: 17406552]

Harata NC, Aravanis AM, Tsien RW. Kiss-and-run and full-collapse fusion as modes of exo-endocytosis in neurosecretion. J Neurochem 2006;97:1546–1570. [PubMed: 16805768]

Haydon PG, Carmignoto G. Astrocyte control of synaptic transmission and neurovascular coupling. Physiol Rev 2006;86:1009–1031. [PubMed: 16816144]

Heuser JE, Reese TS. Evidence for recycling of synaptic vesicle membrane during transmitter release at the frog neuromuscular junction. J Cell Biol 1973;57:315–344. [PubMed: 4348786]

Hirase H, Qian L, Barthó P, Buzsáki G. Calcium dynamics of cortical astrocytic networks in vivo. PLoS Biol 2004;2:E96. [PubMed: 15094801]

Jaiswal JK, Fix M, Takano T, Nedergaard M, Simon SM. Resolving vesicle fusion from lysis to monitor calcium-triggered lysosomal exocytosis in astrocytes. Proc Natl Acad Sci U S A 2007;104:14151–1456. [PubMed: 17715060]

Jourdain P, Bergersen LH, Bhaukaurally K, Bezzi P, Santello M, Domercq M, Matute C, Tonello F, Gundersen V, Volterra A. Glutamate exocytosis from astrocytes controls synaptic strength. Nat Neurosci 2007;10:331–339. [PubMed: 17310248]

Mattheyses AL, Axelrod D. Direct measurement of the evanescent field profile produced by objective-based total internal reflection fluorescence. J Biomed Opt 2006;11:014006. [PubMed: 16526883]

Misenböck G, De Angelis DA, Rothman JE. Visualizing secretion and synaptic transmission with pH-sensitive green fluorescent proteins. Nature 1998;394:192–195. [PubMed: 9671304]

Nadrigny F, Li D, Kemnitz K, Ropert N, Koulakoff A, Rudolph S, Vitali M, Giaume C, Kirchhoff F, Oheim M. Systematic colocalization errors between acridine orange and EGFP in astrocyte vesicular organelles. Biophys J 2007;93:969–980. [PubMed: 17416619]

Ni Y, Malarkey EB, Parpura V. Vesicular release of glutamate mediates bidirectional signaling between astrocytes and neurons. J Neurochem 2007;103:1273–1284. [PubMed: 17727631]

Nimmerjahn A, Kirchhoff F, Kerr JN, Helmchen F. Sulforhodamine 101 as a specific marker of astroglia in the neocortex in vivo. Nat Methods 2004;1:31–37. [PubMed: 15782150]

Pasti L, Volterra A, Pozzan T, Carmignoto G. Intracellular calcium oscillations in astrocytes: a highly plastic, bidirectional form of communication between neurons and astrocytes *in situ*. J Neurosci 1997;17:7817–7830. [PubMed: 9315902]

Pasti L, Zonta M, Pozzan T, Vicini S, Carmignoto G. Cytosolic calcium oscillations in astrocytes may regulate exocytotic release of glutamate. J Neurosci 2001;21:477–484. [PubMed: 11160427]

Rizzuto R, Pozzan T. Microdomains of intracellular Ca^{2+}: molecular determinants and functional consequences. Physiol Rev 2006;86:369–408. [PubMed: 16371601]

Ryan TA, Reuter H. Measurements of vesicle recycling in central neurons. News Physiol Sci 2001;16:10–14. [PubMed: 11390939]

Sala C, Roussignol G, Meldolesi J, Fagni L. Key role of the postsynaptic density scaffold proteins Shank and Homer in the functional architecture of Ca^{2+} homeostasis at dendritic spines in hippocampal neurons. J Neurosci 2005;25:4587–4592. [PubMed: 15872106]

Sankaranarayanan S, Ryan TA. Real-time measurements of vesicle-SNARE recycling in synapses of the central nervous system. Nat Cell Biol 2000;2:197–204. [PubMed: 10783237]

Sankaranarayanan S, Ryan TA. Calcium accelerates endocytosis of vSNAREs at hippocampal synapses. Nat Neurosci 2001;4:129–136. [PubMed: 11175872]

Schweizer FE, Ryan TA. The synaptic vesicle: cycle of exocytosis and endocytosis. Curr Opin Neurobiol 2006;16:298–304. [PubMed: 16707259]

Steyer JA, Almers W. A real-time view of life within 100 nm of the plasma membrane. Nat Rev Mol Cell Biol 2001;2:268–275. [PubMed: 11283724]

Striedinger K, Meda P, Scemes E. Exocytosis of ATP from astrocyte progenitors modulates spontaneous Ca^{2+} oscillations and cell migration. Glia 2007;55:652–662. [PubMed: 17309060]

Thomas D, Lipp P, Tovey SC, Berridge MJ, Li W, Tsien RY, Bootman MD. Microscopic properties of elementary Ca^{2+} release sites in non-excitable cells. Curr Biol 2000;10:8–15. [PubMed: 10660296]

Tovey SC, de Smet P, Lipp P, Thomas D, Young KW, Missiaen L, De Smedt H, Parys JB, Berridge MJ, Thuring J, Holmes A, Bootman MD. Calcium puffs are generic InsP(3)-activated elementary calcium signals and are downregulated by prolonged hormonal stimulation to inhibit cellular calcium responses. J Cell Sci 2001;114:3979–3989. [PubMed: 11739630]

Tse FW, Tse A, Hille B, Horstmann H, Almers W. Local Ca^{2+} release from internal stores controls exocytosis in pituitary gonadotrophs. Neuron 1997;18:121–132. [PubMed: 9010210]

Tsuboi T, Rutter GA. Multiple forms of "kiss-and-run" exocytosis revealed by evanescent wave microscopy. Curr Biol 2003;13:563–567. [PubMed: 12676086]

Tu JC, Xiao B, Yuan JP, Lanahan AA, Leoffert K, Li M, Linden DJ, Worley PF. Homer binds a novel proline-rich motif and links group 1 metabotropic glutamate receptors with IP3 receptors. Neuron 1998;21:717–726. [PubMed: 9808459]

Voglmaier SM, Kam K, Yang H, Fortin DL, Hua Z, Nicoll RA, Edwards RH. Distinct endocytic pathways control the rate and extent of synaptic vesicle protein recycling. Neuron 2006;51:71–84. [PubMed: 16815333]

Volterra A, Meldolesi J. Astrocytes, from brain glue to communication elements: the revolution continues. Nat Rev Neurosci 2005;6:626–640. [PubMed: 16025096]

Wang X, Lou N, Xu Q, Tian GF, Peng WG, Han X, Kang J, Takano T, Nedergaard M. Astrocytic Ca^{2+} signaling evoked by sensory stimulation in vivo. Nat Neurosci 2006;9:816–823. [PubMed: 16699507]

Winship IR, Plaa N, Murphy TH. Rapid astrocyte calcium signals correlate with neuronal activity and onset of the hemodynamic response *in vivo*. J Neurosci 2007;27:6268–6272. [PubMed: 17554000]

Wu MM, Buchanan J, Luik RM, Lewis RS. Ca^{2+} store depletion causes STIM1 to accumulate in ER regions closely associated with the plasma membrane. J Cell Biol 2006;174:803–813. [PubMed: 16966422]

Xiao B, Tu JC, Petralia RS, Yuan JP, Doan A, Breder CD, Ruggiero A, Lanahan AA, Wenthold RJ, Worley PF. Homer regulates the association of group 1 metabotropic glutamate receptors with multivalent complexes of homer-related, synaptic proteins. Neuron 1998;21:707–716. [PubMed: 9808458]

Xu J, Peng H, Kang N, Zhao Z, Lin JH, Stanton PK, Kang J. Glutamate-induced exocytosis of glutamate from astrocytes. J Biol Chem 2007;282:24185–24197. [PubMed: 17584743]

Zenisek D, Steyer JA, Almers W. Transport, capture and exocytosis of single synaptic vesicles at active zones. Nature 2000;406:849–854. [PubMed: 10972279]

Zhang Q, Pangrsic T, Kreft M, Krzan M, Li N, Sul JY, Halassa M, Van Bockstaele E, Zorec R, Haydon PG. Fusion-related release of glutamate from astrocytes. J Biol Chem 2004;279:12724–12733. [PubMed: 14722063]

Zhang Z, Chen G, Zhou W, Song A, Xu T, Luo Q, Wang W, Gu XS, Duan S. Regulated ATP release from astrocytes through lysosome exocytosis. Nat Cell Biol 2007;9:945–953. [PubMed: 17618272]

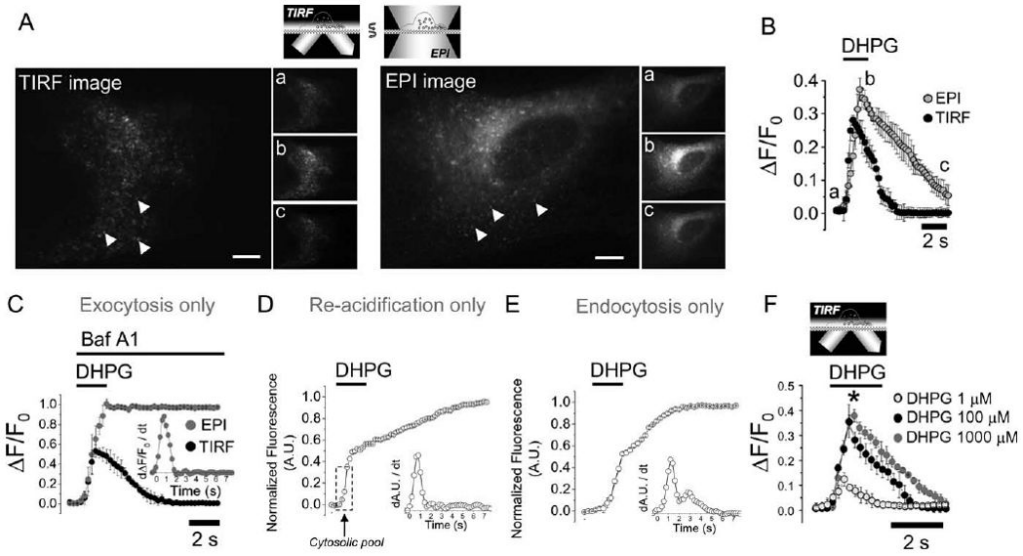

Figure 1.

Characteristics of GPCR-evoked exo-endocytosis and reacidification of SLMVs in astrocytes: whole-cell studies. Experiments were performed under TIRFi and EPIi. ***A***, The two large images represent the same astrocytes transfected with VGLUT1-pHluorin and illuminated with TIRFi or with EPIi. Arrows indicate fluorescent spots corresponding to SLMVs undergoing spontaneous exocytosis. The sequence of images (a, b, c) shows the whole-cell pHF signal before (a), during (b), and after (c) DHPG application under the two illuminations. Scale bars, 10 μm. ***B***, Time course of the DHPG-induced pHF intensity change obtained with TIRFi and EPIi. The curves represent the whole-cell pHF signal, expressed as $\Delta F/F_0$, obtained averaging results from 27 cells. Note that both the rise and the decay times are both faster under TIRFi (rise time: $\tau_{\text{riseTIRF}} = 0.3 \pm 0.088$ s, $\tau_{\text{riseEPI}} = 0.85 \pm 0.18$ s, $p < 0.05$, unpaired *t* test; decay time: $\tau_{\text{decayTIRF}} = 1.63 \pm 0.10$ s, $\tau_{\text{decay EPI}} = 5.4 \pm 0.58$ s, $p < 0.05$, unpaired *t* test). Data points are collected every 200 ms and represent mean values ±SD. ***C***, Same as ***B***, but in the presence of Baf A1 (5μ_{M}; $n = 20$ cells). The rate of spontaneous alkalinization (TIRFi, 0.038 ± 0.005 $\Delta F/F_0$; EPIi, 0.057 ± 0.01 $\Delta F/F_0$) was calculated in the prestimulus period and subtracted from the curves. Note that the curve under EPIi represents a cumulative curve of exocytosis; the curve under TIRFi is not significantly different from the one obtained in the absence of Baf A1 ($\tau_{\text{riseTIRFBaf}} = 0.25 \pm 0.092$ s vs $\tau_{\text{riseTIRF}} = 0.3 \pm 0.088$ s; $\tau_{\text{decayTIRF Baf}} = 1.59 \pm 0.09$ s vs $\tau_{\text{decayTIRF}} = 1.63 \pm 0.1$ s, $p < 0.05$, unpaired *t* test). In the inset, curves represent the first derivative ($d\Delta F/F_0/dt$) of the EPI curve and provide the temporal distribution of the exocytic events. ***D***, Cumulative curve of estimated reacidification obtained by subtracting the normalized curves of the pHF signal obtained under EPIi in the absence of Baf A1 (curve in ***B***) from the curve in the presence of the drug (curve in ***C***). Curves in ***B*** and ***C*** were normalized to the maximum fluorescence obtained under EPIi in the presence of Baf A1 for each cell. In the inset, curves represent the first derivative (dA.U./d*t*) of the curve and provide the temporal distribution of the reacidification processes. Note that during the first 800 ms after the stimulus, the reacidification is detected only by EPIi and involved pool of vesicles located out of the EW field. ***E***, Cumulative curve of estimated endocytosis (movement out of EW field) obtained by subtracting the normalized curves of the pHF signal obtained under TIRFi and under EPIi both in the presence of Baf A1 (curves in ***C***). Curves in ***C*** were normalized to the maximum fluorescence obtained under EPIi and TIRFi, respectively, in the presence of Baf A1 for each cell. In the inset, curves represent the first derivative (dA.U./d*t*) of the curve and provide the temporal distribution of the endocytic events. ***F***, Curves represent the pHF signal obtained under TIRFi in response to different DHPG concentrations expressed as $\Delta F/F_0$(1, 100, 1000

μ_M each;n = 10 cells;0.115 ± 0.025, 0.357 ± 0.048, 0.39 ± 0.025 $\Delta F/F_0$, respectively). The $\Delta F/F_0$ response and the rates of recovery to 100 μ_M DHPG is significantly different from the response to 1 μ_M DHPG but not from the response to 1000 μ_M DHPG (1, 100, 1000 μ_M: 0.06 ± 0.01, 0.12 ± 0.05, 0.1 ± 0.04 A.U./s, respectively; *p < 0.05, one-way ANOVA). Note that 1 mM DHPG did not cause more fluorescence increase than 100 μ_M because the exocytosis is most probably saturated (supplemental Fig. 4 SI, available at www.jneurosci.org as supplemental material).

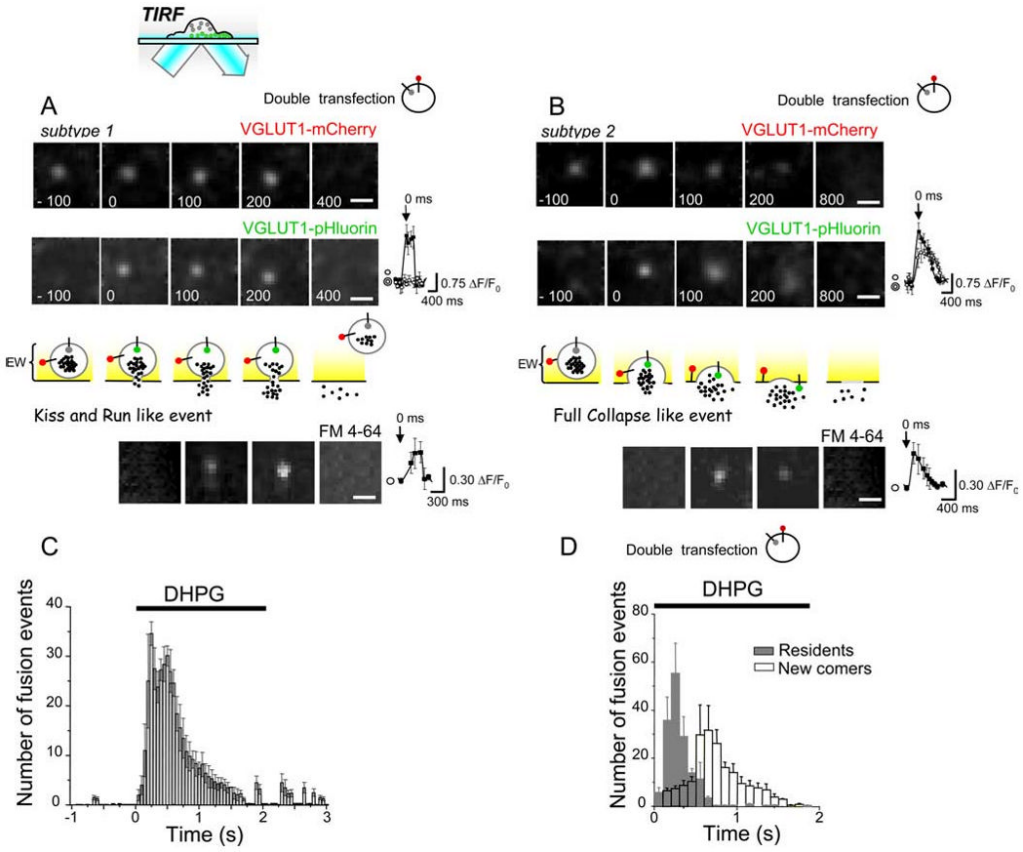

Figure 2.

Evidence for two modes of exo-endocytosis: single vesicle studies. Experiments were performed under TIRFi. ***A***, Images and schematic diagram illustrate a typical subtype 1 fusion event. The first two sequences of images from top to bottom represent the dynamics of mCF and pHF signals taken in parallel from the same SLMV undergoing a fusion event. Top right, Time course of pHF changes (average of 112 different SLMVs, $n = 26$ cells) in a small circle enclosing the fluorescent spot (filled circles) and in a concentric annulus around the circle (open circles). The scheme below summarizes the behavior of the two fluorescent markers during a subtype 1 fusion that is consistent with the kiss-and-run type of fusion. The color code for the pHF signal is gray when the signal is off and green when it is on. The last sequence of images at the bottom shows the time course of FM 4–64 loading during a subtype 1 fusion event. Images are temporally aligned with the pHF sequence. Bottom right, Time course of FM 4–64 fluorescence changes (average of 140 different SLMVs, $n = 12$ cells) measured in a small circle enclosing the fluorescent spot (filled circles). Scale bars, 0.5 μm. ***B***, Images and schematic diagram illustrate a typical subtype 2 fusion event. The figure is organized as in ***A***, but notice the different timing of the images, the different time courses of pHF and FM 4–64 signals, and the different behavior of the two fluorescent markers in the scheme representing a subtype 2 fusion. Such fusion is consistent with the full collapse type of fusion. ***C, D***, Temporal distribution of fusion events evoked by DHPG application (2 s, 100 μ_M). ***C***, Each individual histogram represents the number (mean ± SD) of fusion events detected in a 50-ms-long frame ($n = 34$ cells). ***D***, Temporal distribution of fusion events for resident vesicles (gray) and for newcomer vesicles (white). White frames overlapped with gray histograms highlight newcomer fusion events at times when resident fusion events prevail. Each histogram represents the number (mean ± SD) of fusion events counted in a 100-ms-long frame ($n = 20$ cells).

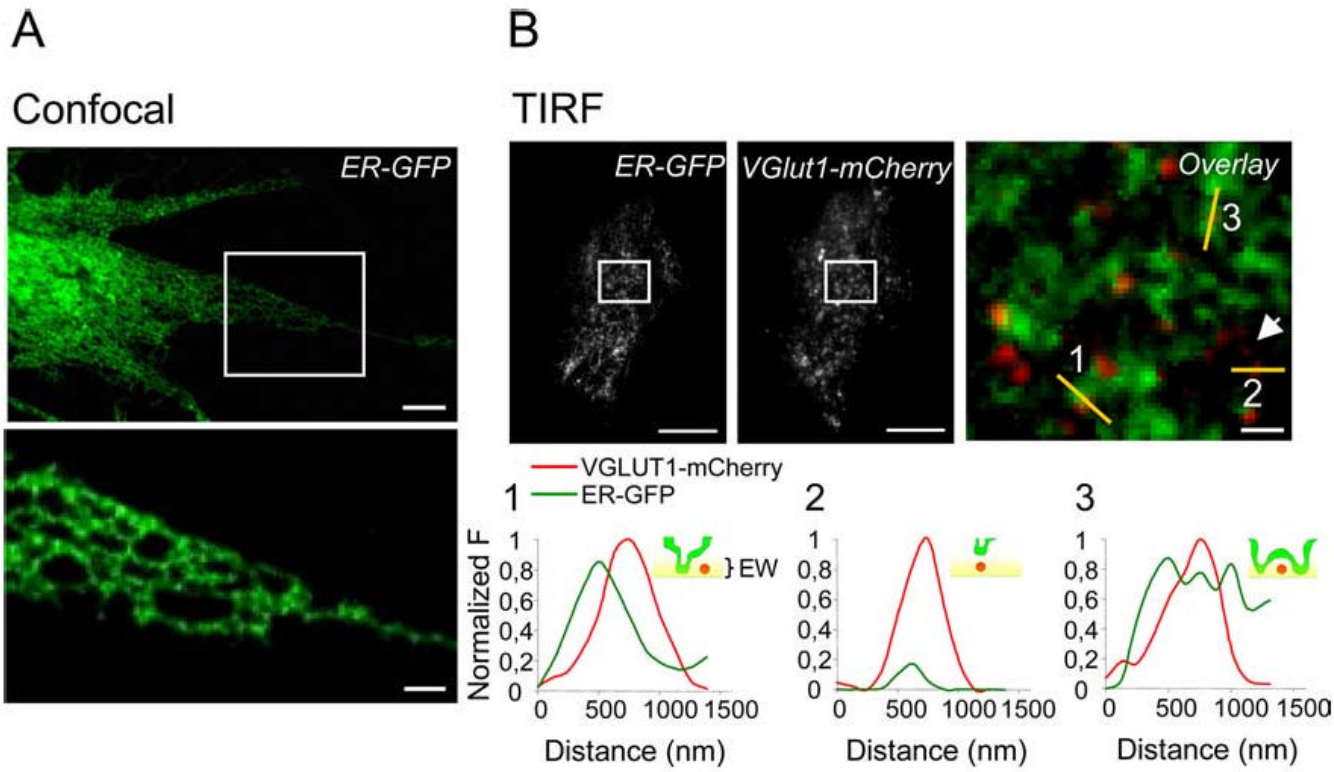

Figure 3.

Spatial relationship between ER tubuli and SLMVs in the submembrane compartment. ***A***, Confocal image of an astrocyte expressing ER-EGFP. Scale bar, 5 μm. The magnification of the boxed region (bottom) shows the distribution of ER tubuli in a fine process. Scale bar, 2 μm. ***B***, Top, TIRF images of an astrocyte expressing ER-EGFP and VGLUT1-mCherry. Scale bars, 10 μm. The high magnification of the boxed region (top right) represents the overlay of the two images. Scale bar, 1 μm. The discrete structures in green represent extremities of the ER tubuli approaching the plasma membrane (average, 248625 ± 47201 nm^2/structure; n = 283 structures analyzed). The red dots are SLMVs resident in the EW field. ER tubules surround almost all of the vesicles in the field; only one vesicle (arrow) has no ER tubules within 1.5 μm. Bottom, Curves represent line intensity profiles calculated across green structures and red puncta in three representative cases corresponding to the numbered yellow lines in the overlay image. Diagrams in the insets illustrate the spatial distribution of ER tubules (green) and SLMVs (red) in the EW field for each representative case.

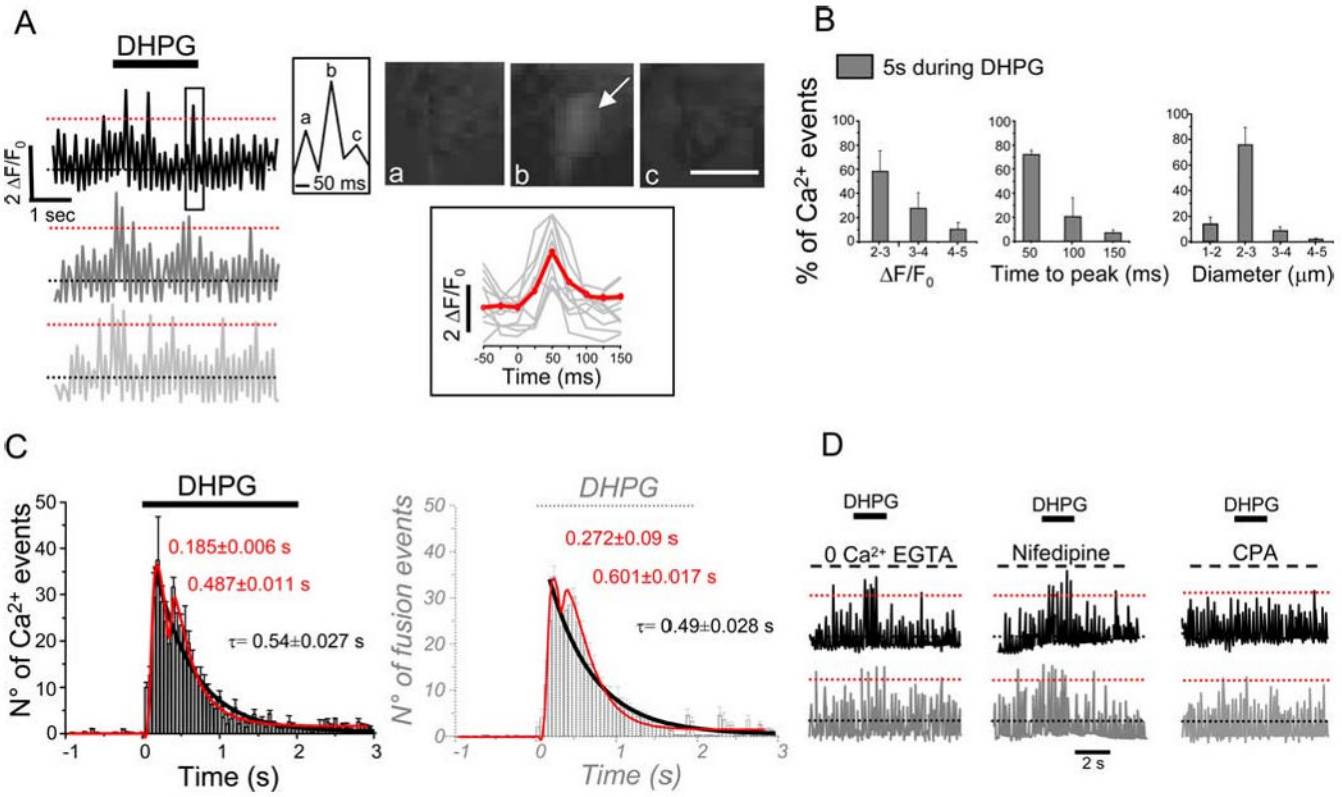

Figure 4.

GPCR-evoked submembrane Ca^{2+} events. Experiments performed under TIRFi. ***A***, Right, top to bottom, Three representative traces of submembrane Ca^{2+} changes, each one showing periods before, during, and after application of DHPG (100 μ_M, 2 s). The black dotted lines in the traces indicate the average basal fluorescence value; the red dotted lines indicate the fluorescence value exceeding the basal value by twofold. On the right of the traces, the high magnification of the boxed region shows a typical fast submembrane Ca^{2+} event. Farther on the right are presented the TIRF images (filtered with low pass filter) corresponding to that Ca^{2+} event (a–c). Scale bar, 2 μm. In the inset below the images, traces represent an expanded view of temporally aligned Ca^{2+} events (gray) and of their average (red) obtained from 467 ROIs (n = 3 cells) located in different cellular regions. Data points were collected every 25 ms (sampling rate, 40 Hz). ***B***, Frequency histograms providing information on the features of submembrane Ca^{2+} events in terms of amplitude ($\Delta F/F_0$), time-to-peak (milliseconds), and diameter of spread in the x–y plane (μm) during 5 s of DHPG. Data obtained from 6706 Ca^{2+} events (n = 12 cells) were put into bins and their frequency expressed as percentage of the total number of events. ***C***, Temporal distribution of the Ca^{2+} events (left) compared with the distribution of the fusion events (ghost on the right). Each histogram represents the number (mean ± SD) of events counted in a 50-ms-long frame (n = 25 cells). Red lines represent double exponential fits (peak times are written in red on top of each peak), and black lines represent single exponential decay (τ_{decays} are written on the side in black). ***D***, Representative Ca^{2+} traces of an experiment as in ***A***, but in which cells were exposed to an external medium either lacking Ca^{2+} (0 Ca^{2+} with 5 mM of EGTA; n = 8 cells), or containing nifedipine (3 μ_M; n = 10 cells), or CPA (10 μ_M, 15 min; n = 7 cells).

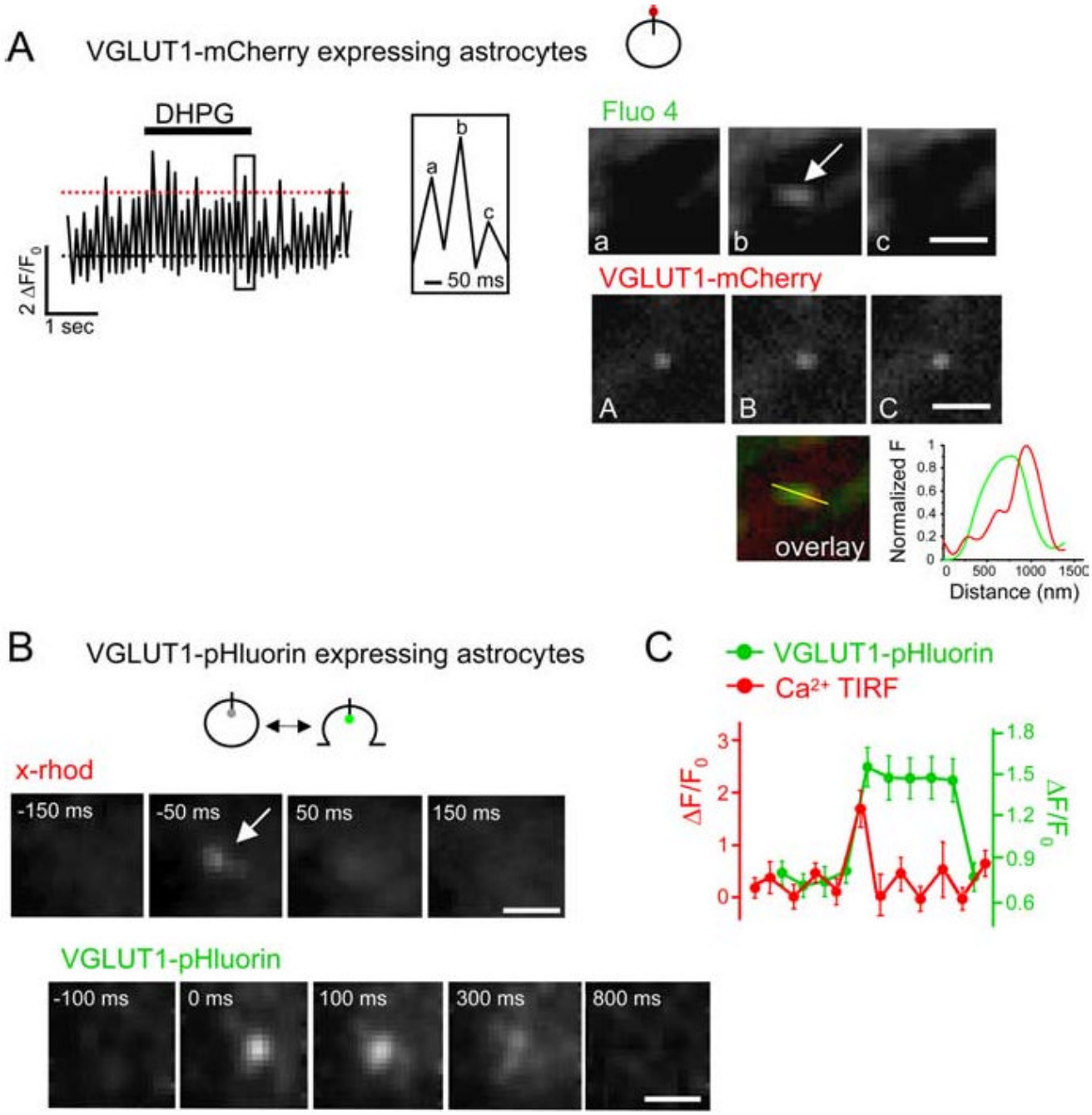

Figure 5.

Spatial-temporal correlation of submembrane Ca^{2+} events and SLMV fusion events. ***A***, Spatial correlation of Ca^{2+} events and SLMV fusion events. Left, Representative trace of fast submembrane Ca^{2+} events occurring in a ROI centered on an SLMV expressing VGLUT1-mCherry. The high magnification (right) shows the kinetics of the Ca^{2+} event in the boxed region. Right, top to bottom, Sequence of TIRF images of the same Ca^{2+} event (a–c), corresponding sequence of the SLMV (A–C), and colored overlay showing colocalization of the Ca^{2+} event with the vesicle. The diagram on the side of the overlay illustrates the spatial distribution of the Ca^{2+} event (green) and of the SLMV (red) in the EW field. Scale bars, 2 μm. ***B, C***, Temporal correlation of Ca^{2+} events and SLMV fusion events. ***B***, Representative

sequences of TIRF images monitoring a Ca^{2+} event (top) and a subtype 2 fusion event of a VGLUT1-pHluorin-expressing SLMV (bottom) occurring in the same ROI. Ca^{2+} events are monitored as changes in fluorescence of the red dye, x-rhod. Note that the Ca^{2+} event precedes vesicle fusion by one frame (−50 ms). Scale bars, 1 μm. ***C***, Correlated time course of Ca^{2+} events and SLMV fusion events. Data points (mean ± SD) were collected every 50 ms. The red curve represents the average kinetics of the Ca^{2+} event calculated by a pool of 35 Ca^{2+} events (n = 10 cells). The black curve represents the average kinetics of the fusion event occurring in temporal correlation with the Ca^{2+} event in the same ROIs. The two curves were normalized and aligned: as a result, the peak of the Ca^{2+} event precedes by 50 ms the peak of the SLMV fusion event.

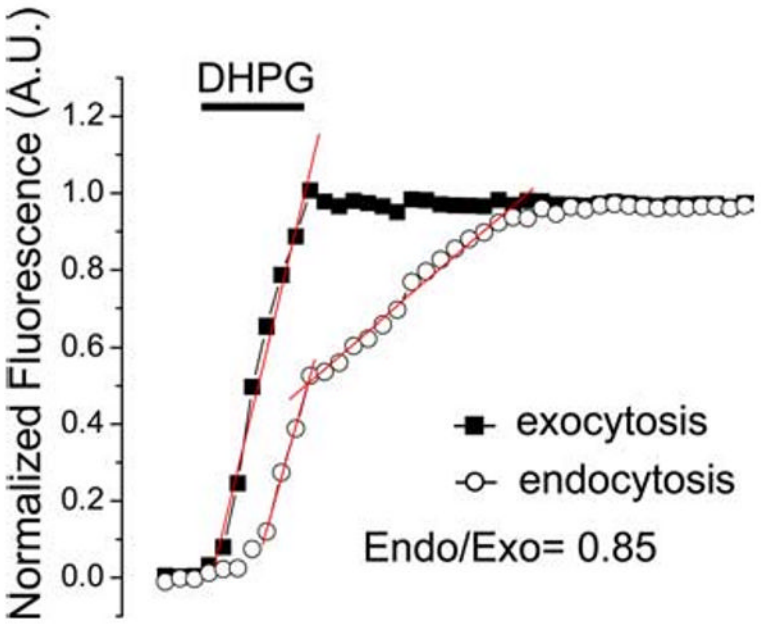

Figure 6.

Rate of SLMV exocytosis and endocytosis in astrocytes. Curves representing kinetics of exocytosis (same as in Fig. 1C but normalized to the maximal fluorescence value in the presence of Baf A1, filled squares) and of endocytosis (same as in Fig. 1D, open circles) were temporally aligned with respect to the start of the stimulus. Red lines represent linear fits to the rising phases of the two curves. The ratio of the slopes of endocytosis and exocytosis (based on linear fits to the rising phases) provides an estimate of the speed of endocytosis relative to that of exocytosis during the stimulus ($Endo_{speed}$ = 0.85 Exo_{speed}).